Journal of Applied Physics

High thermopower and power factors in $EuFeO_3$ for high temperature thermoelectric applications: A first-principles approach

Cite as: J. Appl. Phys. **128**, 155101 (2020); https://doi.org/10.1063/5.0016071
Submitted: 01 June 2020 . Accepted: 01 October 2020 . Published Online: 15 October 2020

P. Iyyappa Rajan, Carlos Baldo, Enamullah, S. Mahalakshmi, R. Navamathavan, and T. Adinaveen

Journal of Applied Physics ARTICLE scitation.org/journal/jap

High thermopower and power factors in $EuFeO_3$ for high temperature thermoelectric applications: A first-principles approach

Cite as: J. Appl. Phys. **128**, 155101 (2020); doi: 10.1063/5.0016071
Submitted: 1 June 2020 · Accepted: 1 October 2020 ·
Published Online: 15 October 2020

P. Iyyappa Rajan,[1,a)] Carlos Baldo, III,[1,2] Enamullah,[3] S. Mahalakshmi,[4,a)] R. Navamathavan,[5,a)] and T. Adinaveen[6]

AFFILIATIONS

[1]Asia Pacific Center for Theoretical Physics, POSTECH Campus, Pohang, 37673, South Korea
[2]Department of Physics, Mapua University, Intramuros, Manila 1002, Philippines
[3]Department of Physics, School of Applied Sciences, University of Science and Technology, Meghalaya, Ri Bhoi 793101, India
[4]Chemistry Division, School of Advanced Sciences, Vellore Institute of Technology (VIT), Chennai Campus, Chennai 600127, India
[5]Division of Physics, School of Advanced Sciences, Vellore Institute of Technology (VIT), Chennai Campus, Chennai 600127, India
[6]Department of Chemistry, Loyola College (Autonomous), Nungambakkam, Chennai 600034, India

[a)]**Authors to whom correspondence should be addressed:** rajanselvam29@gmail.com; mahalakshmi.sn@vit.ac.in; and navamathavan.r@vit.ac.in

ABSTRACT

Thermoelectric materials that can work at operating temperatures of $T \geq 900$ K are highly desirable since the key thermoelectric factors of most thermoelectric materials degrade at high temperatures. In this work, we investigate the high temperature thermoelectric performance of $EuFeO_3$ using a combination of first-principles methods and semi-classical Boltzmann transport theory. High temperature thermoelectric performance is achieved owing to the presence of corrugated flatbands in the valence band region and extremely flatbands in the conduction band region. The lowest energetic structure of $EuFeO_3$ lies within a G-type antiferromagnetic configuration, and the effect of compressive and tensile strains (−7% to +7%) along the (*a, b*) axes on thermoelectric performance is systematically analyzed. An extremely high value of the Seebeck coefficient (more than 1000 μV/K) is consistently recorded in the high temperature region between 900 K and 1400 K in this material. Furthermore, electrical conductivities and power factors are high and electronic thermal conductivities are low in the considered range of temperatures. The calculated theoretical minimum lattice conductivity is small, estimated at around 1.47–1.54 W m^{-1} K^{-1}. A compressive strain of −3% is revealed to be the optimum level of strain for enhancing the key thermoelectric factors. Overall, p-type doping shows better thermoelectric performance than n-type doping in $EuFeO_3$.

I. INTRODUCTION

Growing interest in the study of thermoelectrics (TEs) is driven by the need for alternative sources of electrical power due to the increasing demand for energy and the depletion of non-renewable resources.[1–4] TE materials have become viable candidates due to their capability of converting waste heat into useful electrical energy.[2,4,5] New, high performance TE materials have been reported and can generally be classified into three categories based on their working temperature: low temperature ($T < 500$ K) materials such as Bi_2Te_3, medium temperature (500 K $\leq T \leq$ 900 K) materials such as PbTe, and high temperature ($T \geq 900$ K) materials such as SiGe alloys.[6] The availability of TE materials operating at low and mid-temperatures is larger than that for TE materials operating at high temperatures. Nevertheless, TE materials running at $T \geq 900$ K are used in key technologies such as in the operation of deep-spacecraft missions, nuclear reactors, and high temperature industrial reactors.[1] A well-known example is the use of SiGe thermoelectrics in the spacecraft designs of NASA in the Voyager 1, Voyager 2, and Galileo space probes.[1]

Thus, research into new high temperature TE materials with superior properties is receiving a considerable amount of attention. In this work, we investigate exceptional TE performance in a

distorted perovskite-based material through first-principles density functional theory (DFT) calculations. Perovskite oxides, with a general formula ABO_3, display a myriad of interesting properties such as magnetoresistance, superconductivity, electrical conductivity, thermal stability, low dielectric loss, and ferroelectricity.[7] Additionally, rare earth orthoferrites, usually expressed as $RFeO_3$, are known to be distorted perovskites with extensive applications in solid oxide fuel cells, gas sensors, and photocatalysis.[8–11] $EuFeO_3$ is one such compound from the $RFeO_3$ family that belongs to the orthorhombic crystal system. The Eu ions occupy a dodecahedral A site and the Fe ions occupy an octahedral B site. The unit cell contains a corner sharing FeO_6 octahedron, resulting in a 3D perovskite structure.[7] The rotation patterns of a strained $EuFeO_3$ and other perovskite films have been studied and reported by Choquette *et al.*[12] In an earlier paper, Choquette *et al.*[13] observed the development of $EuFeO_3$ thin films by molecular beam epitaxy, and the $EuFeO_3$ bandgap displayed a blue shift in comparison to $LuFeO_3$. Structural elucidation of rare earth orthoferrites was carried out by Marezio *et al.*, who found that in moving from $LuFeO_3$ to $SmFeO_3$, the distortion of FeO_6 octahedron was negligible and nearly constant.[14] Other than the above-mentioned reports, a few studies have been undertaken for $EuFeO_3$. Experimental studies of $EuFeO_3$ as a TE material have not been performed so far, and we have not found any DFT calculation reports on $EuFeO_3$ that take into account the correct electronic structure. In this work, we present the effectiveness of $EuFeO_3$ as a potential high temperature TE material with the help of first-principles DFT calculations combined with semi-classical Boltzmann transport theory.

II. CALCULATION DETAILS

A conventional unit cell of $EuFeO_3$, as illustrated in Fig. 1(a), follows an orthorhombic structure with space group number 62 (Pnma) containing 4 Eu atoms, 4 Fe atoms, and 12 O atoms. First-principles DFT calculations were implemented using the Vienna *ab initio* simulation package (VASP),[15,16] with inputs derived from experimentally resolved x-ray diffraction data[14] for structural optimization. We employed the projector augmented wave (PAW) method,[16,17] and a plane wave kinetic energy cutoff of 600.00 eV was used. For the exchange correlation effects, we utilized the Perdew–Burke–Ernzerhof (PBE) potentials, based on the generalized gradient approximation (GGA).[18] The DFT calculations were carried out in such a way that the exact electronic structure and the ground state magnetic configuration were appropriately realized. This was done by including the 4f electron states as valence electrons, in addition to the 5s, 5p, and 6s states for Eu, 3d, and 4s states for Fe, and 2s and 2p states for O atoms. To get the appropriate bandgap, we followed the PBE + U approach proposed by Dudarev *et al.*,[19] with an effective Hubbard parameter (U_{eff}) of 5.0 for 3d states and 11.0 for 4f states. The high U_{eff} value of 11.0 eV for Eu 4f states makes the relaxation convergence easier. This value for U_{eff} has been similarly used in Ref. 20 to treat Gd 4f states in gadolinium-doped $BiFeO_3$, which has a similar number of 4f electrons as europium. Brillouin zone integration was chosen to be the Γ-point with $6 \times 6 \times 4$ k-points for relaxation and $10 \times 10 \times 10$ k-points for transport calculations. The $EuFeO_3$ orthorhombic structure was relaxed using the conjugate gradient algorithm method,[21] wherein only the structural atomic positions underwent the relaxation, not the experimental lattice constants. The total energy convergence criterion was fixed at 10^{-6} eV and the Hellmann–Feynman forces were relaxed below 0.01 eV/Å. The total energy of the different magnetic configurations of $EuFeO_3$ (FM, A-type AFM, C-type AFM, and G-type AFM) was examined using spin-polarized calculations, while the non-magnetic configuration was examined through non-spin-polarized calculations. The results revealed that the lowest energy lies within the G-type AFM configuration of $EuFeO_3$. The stability order was found to be as follows: non-magnetic > FM > A-type AFM > C-type AFM > G-type AFM. Therefore, the G-type AFM structure of orthorhombic $EuFeO_3$ was considered for all the calculations. After relaxing the structure of $EuFeO_3$ to the ground state, tensile and compressive bi-axial strains of +7%, +5%, +3%, +1%, −1%, −3%, −5%, and −7% were applied along the in-plane a and b axes and the relaxation was further carried out. The basis of applying bi-axial tensile and compressive strains in $EuFeO_3$ is discussed in Sec. III. The final output structural parameters obtained from the DFT calculations are listed in Table S1 in the supplementary material. These structural parameters were then fed into the BoltzTrap2 program.[22]

The thermoelectric performance of a thermoelectric material is determined by analyzing its transport properties, e.g., the Seebeck coefficient (S), electrical conductivity (σ), and electronic thermal conductivity (κ_e). We calculated these coefficients using a semi-classical Boltzmann transport equation under a constant relaxation time (τ) approximation (cRTA) and rigid band approximation as implemented in BoltzTrap2 code.[22] The code relies on a Fourier expansion of the electronic band structure energies along with the space group symmetry information. These initial data were obtained from first-principles simulations, which were required as input data for the code. Thereafter, the electrical conductivity tensor ($\sigma_{\gamma\delta}$) could be obtained by performing the Fourier expansion as

$$\sigma_{\gamma\delta}(i,k) = e^2 \tau_{i,k} v_\gamma(i,k) v_\delta(i,k), \tag{1}$$

where e is the electronic charge, $\tau_{i,k}$ represents the electron relaxation time (from the electron–phonon coupling), and $v_\gamma(i,k)$ is the γ-component of the group velocity for an electron in band index I,

$$v_\gamma(i,k) = \frac{1}{\hbar}\frac{\partial \in_{i,k}}{\partial k_\gamma}. \tag{2}$$

From the previous electrical conductivity matrix, it is possible to calculate the relevant transport tensor, which depends upon the temperature (T) and the chemical potential (μ). Hence, the final expressions for σ, v, S, and κ_e tensors are

$$\sigma_{\gamma\delta}(T,\mu) = \frac{1}{(2\pi)^3}\sum_i \int \sigma_{\gamma\delta}(i,k)\left(-\frac{\partial f(T,\mu)}{\partial \in}\right) dk, \tag{3}$$

$$v_{\gamma\delta}(T,\mu) = \frac{1}{(2\pi)^3 T}\sum_i \int \sigma_{\gamma\delta}(i,k)[\in(k) - \mu]\left(-\frac{\partial f(T,\mu)}{\partial \in}\right) dk, \tag{4}$$

$$\kappa_{e,\gamma\delta}(T,\mu) = \frac{1}{(2\pi)^3 T}\sum_i \int \sigma_{\gamma\delta}(i,k)[\in(k) - \mu]^2\left(-\frac{\partial f(T,\mu)}{\partial \in}\right) dk, \tag{5}$$

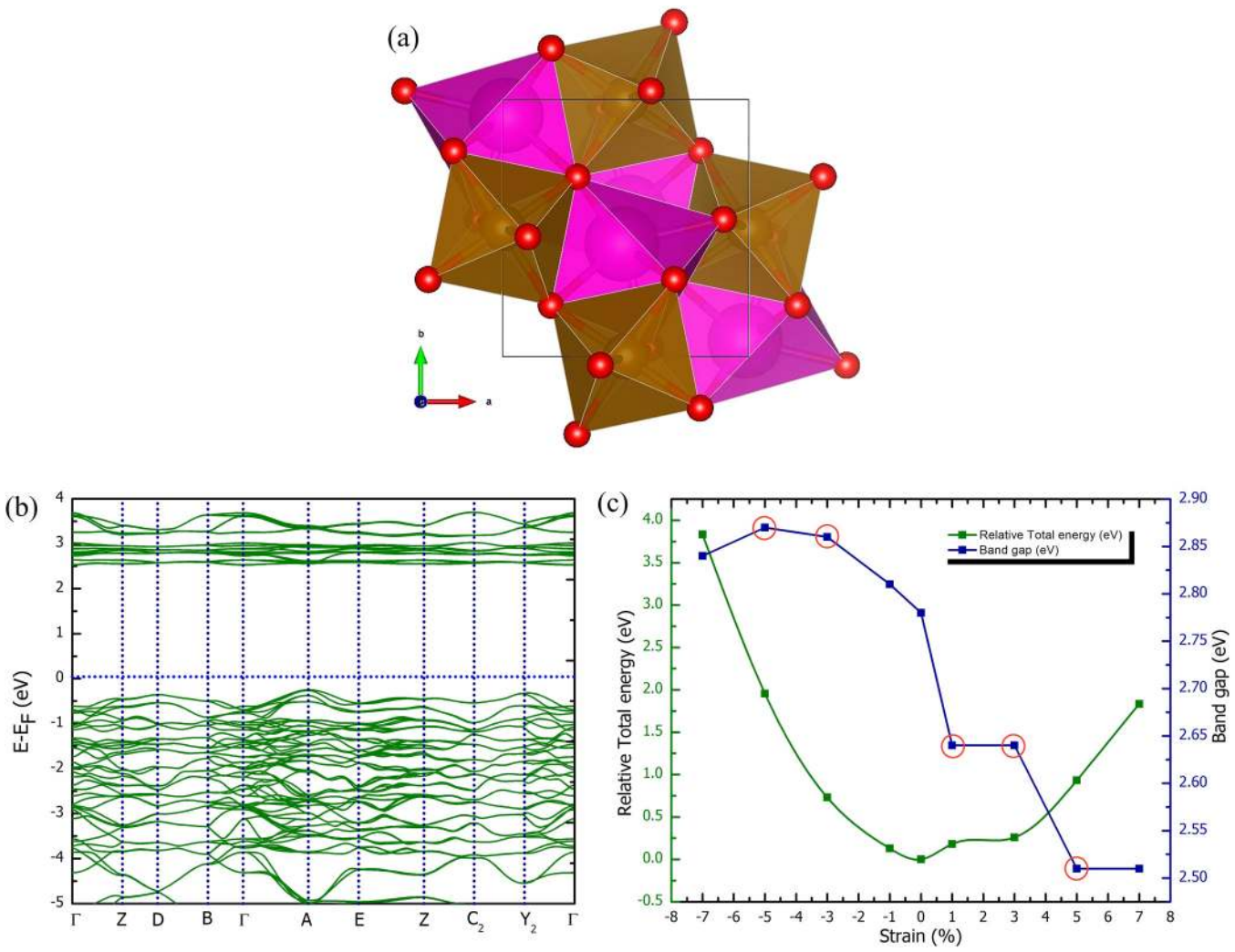

FIG. 1. (a) Crystal structure of an orthorhombic $EuFeO_3$ (Eu, rose; Fe, brown; and O, red). (b) Electronic band structure of $EuFeO_3$ under zero strain. (c) Effect of strain on the total energy and bandgap of $EuFeO_3$, where the encircled points are direct bandgaps and the rest of the points are indirect bandgaps. The negative percentage values correspond to compressive strain and positive values to tensile strain.

and

$$S_{ij}(T,\mu) = \sum_{\gamma} (\sigma^{-1})_{\gamma i} v_{\gamma j}, \tag{6}$$

where f represents the Fermi–Dirac distribution function.

III. RESULTS AND DISCUSSION

A. Band structure of $EuFeO_3$

The electronic band structures are presented in Fig. 1(b). The total density of states (DOS) of $EuFeO_3$ is presented in Fig. S1 in the supplementary material. The band structures of $EuFeO_3$ were calculated within the band path using the SeeK-path software tool.[23]

Figure 1(c) shows the effect of strain on the relative total energy and bandgap of $EuFeO_3$. The encircled points in Fig. 1(c) are direct bandgaps, and the other points are indirect bandgaps. There is an increase in the bandgap as the applied strain moves from tensile to compressive strain. However, there is a threshold value at which a greater compressive strain has no effect in the bandgap. The reason for the increasing bandgap due to the compressive strain can be seen in the band structures of $EuFeO_3$ shown in Figs. 2(a)–2(c). Here, we find that the valence band maximum (VBM) moves downward away from the Fermi level particularly at the Γ and A points, whereas the conduction band minimum

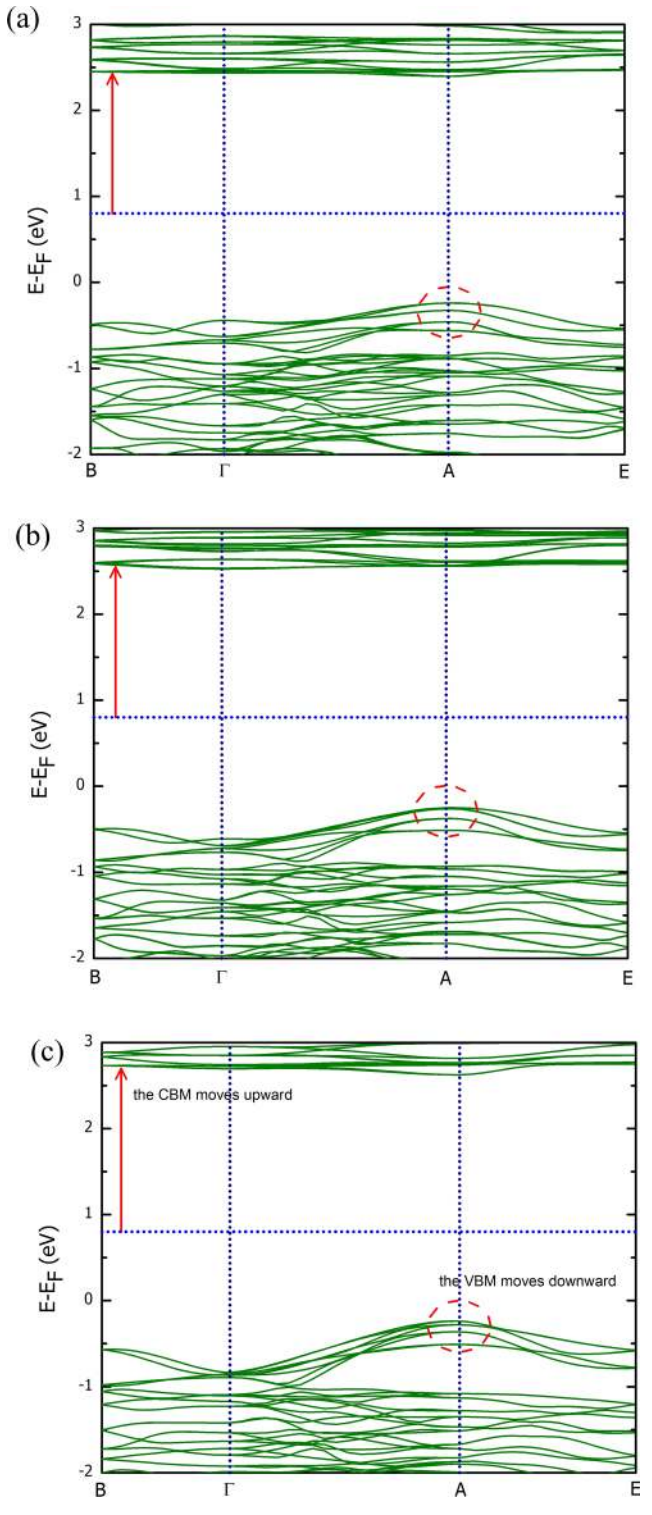

FIG. 2. Magnified view of the electronic band structure of $EuFeO_3$ under (a) 3% tensile, (b) zero, and (c) 3% compressive strain.

(CBM) moves upward as we change from 3% tensile to 3% compressive strain. This, in effect, widens the bandgap of the material. At zero strain, a large bandgap of 2.78 eV was calculated, which was close to the experimental value of 2.5 eV.[13] Though, it appears that our calculations may have overestimated the bandgap of $EuFeO_3$, there have been a few cases, such as in PbSe and Bi_2Se_3,[24] where the PBE approach has overestimated the bandgap. Heyd–Scuseria–Ernzerhof (HSE) calculations could have been used to calculate the accurate bandgap, but this was too computationally expensive for our system. Nevertheless, we have shown that the calculated value for the bandgap using PBE potentials is close to the recently reported bandgap of epitaxial $EuFeO_3$ thin films in Ref. 13. In addition, it is possible that this overestimation might not be hugely associated with the PBE potentials that deal with a perfect crystal structure. In many cases, the synthesized samples may have some structural/crystal defects (vacancies) that shift the bandgap toward the visible region. From the band structure diagrams in Fig. 1(b), we find that the valence band of the material displays flatness with some local peaks and troughs. Such a band structure with multi-valley features is referred to as corrugated flat bands as discussed in Ref. 25. In that study, Mori *et al.* reported that the topmost valence band in $PtSb_2$, derived from first-principles calculations, is almost entirely from Sb 5p orbitals, it lacks d orbital character, and is therefore non-bonding in nature. Similar cases have been reported, for instance, in Refs. 26 and 27. In our case, the corrugations found in the VBM are brought about by the significant hybridization of Fe and Eu d states with O 2p states. The absence of such a hybridization process is the reason why the CBM is nearly flat, which is primarily attributed to the Eu 4f and Fe 3d states. The existence of such corrugated flatbands in the VBM results in multiple Fermi surface pockets scattered throughout the Brillouin zone.[25] These multiple Fermi pockets arise due to the flat nature of the conduction band and the corrugated flatness of the valence band. The presence of multiple Fermi surfaces with high group velocity gives rise to an enhanced Seebeck coefficient and a high electric conductivity,[25] which leads to a high power factor. Aside from the extremely flat and corrugated flatbands, a large bandgap further ensures a high Seebeck coefficient.[26] This was similarly observed in Ref. 27, where nitrogenated holey graphene displayed flatbands near the Fermi level and showed a higher bandgap, thereby giving rise to a large Seebeck coefficient. The presence of these features in the band structure, combined with its large bandgap, strongly supports our idea that $EuFeO_3$ is a promising TE material, with a high Seebeck coefficient and a large electrical conductivity, as shown in the following sections. An enhanced power factor is required for a good thermoelectric material as it can produce more power.

B. Thermoelectric properties

The effectivity of a TE material is commonly measured using the figure of merit ZT,

$$ZT = \frac{S^2 \sigma T}{\kappa}. \tag{7}$$

Here, we define the following thermoelectric properties: S is the Seebeck coefficient, σ is the electrical conductivity, and κ is the

total thermal conductivity of the material. κ is further expressed as the sum of the electron (κ_e) and lattice (κ_l) contributions to the thermal conductivity. Recently, TE performance has been measured using another TE quantity, the power factor *PF*, which can be computed directly as

$$PF = S^2\sigma. \tag{8}$$

Thus, we can say that an efficient TE candidate is a material that has a large Seebeck coefficient, a high electrical conductivity, a high power factor, and a sufficiently low thermal conductivity. In this work, we demonstrate the potential TE capability of $EuFeO_3$ at high temperatures by highlighting its remarkable TE properties. We begin with its high Seebeck coefficient obtained for $T \geq 900$ K, as shown in Fig. 3(a). As seen in this graph, the calculated values of *S* are found to be at least 800 μV/K across all given temperatures and strains. Additionally, the calculation is employed using different values of strain, which varies from tensile (+7%, +5%, +3%, +1%) to compressive (−7%, −5%, −3%, −1%). From Fig. 3(a), it can be seen that *S* is greatest across all temperatures when a compressive strain −3% is applied, as indicated by the blue arrows. However, application of tensile strain lowers the Seebeck coefficient. This effect of the strain on the Seebeck coefficient can be described in two modes, which are both traced to the band structure. To illustrate this, we show in Figs. 2(a)–2(c) the band structures of $EuFeO_3$ under 3% tensile, zero, and 3% compressive strains. First, the presence of compressive strain enhances the corrugations in the VBM and the flatness in the CBM. As can be seen in the band structures, there are more corrugations (local peaks and troughs) in the valence band as we move from tensile toward compressive strain. These enhanced corrugations near the Fermi level, as discussed earlier, induce a greater velocity difference in the carriers, which consequently leads to an improvement in the Seebeck coefficient. Additionally, the increase in *S* due to the 3% compressive strain is brought about by the overlapping of multiple bands in the VBM and the CBM. As discussed earlier, the bandgap of the material increases as the applied strain is altered from tensile to 3% compressive strain, where it reaches its maximum value. This increase in the bandgap can also improve the Seebeck coefficient. In our work, we limit the discussion to the two cases of zero strain and 3% compressive strain. As shown in Fig. 1(c), the relative total energies of 5% and 7% compressive strains are significantly high compared to that of zero strain. Therefore, we did not consider these strains for comparison. In Figs. 3(b) and 3(c), we show the effect of doping on *S* for $T \geq 900$ K under zero and 3% compressive strain, respectively. For a given curve of *S* vs $\mu - E_F$, the kind of doping in the material can be deduced from the sign of *S*: negative values indicate n-type doping and positive values indicate p-type doping. Through careful inspection, we find that for both strain cases, p-type doping shows slightly higher values of *S* than n-type doping for temperatures above 1000 K. As observed earlier, a larger *S* is achieved for the −3% compressive strain than for the unstrained case. There is no doubt that high *S* is attainable from $EuFeO_3$ at high temperatures. Nevertheless, we have discovered that a similar magnitude of *S* can also be obtained, even at relatively low temperatures. We show this in Fig. S2 in the supplementary material. Here, we briefly examine how *S*

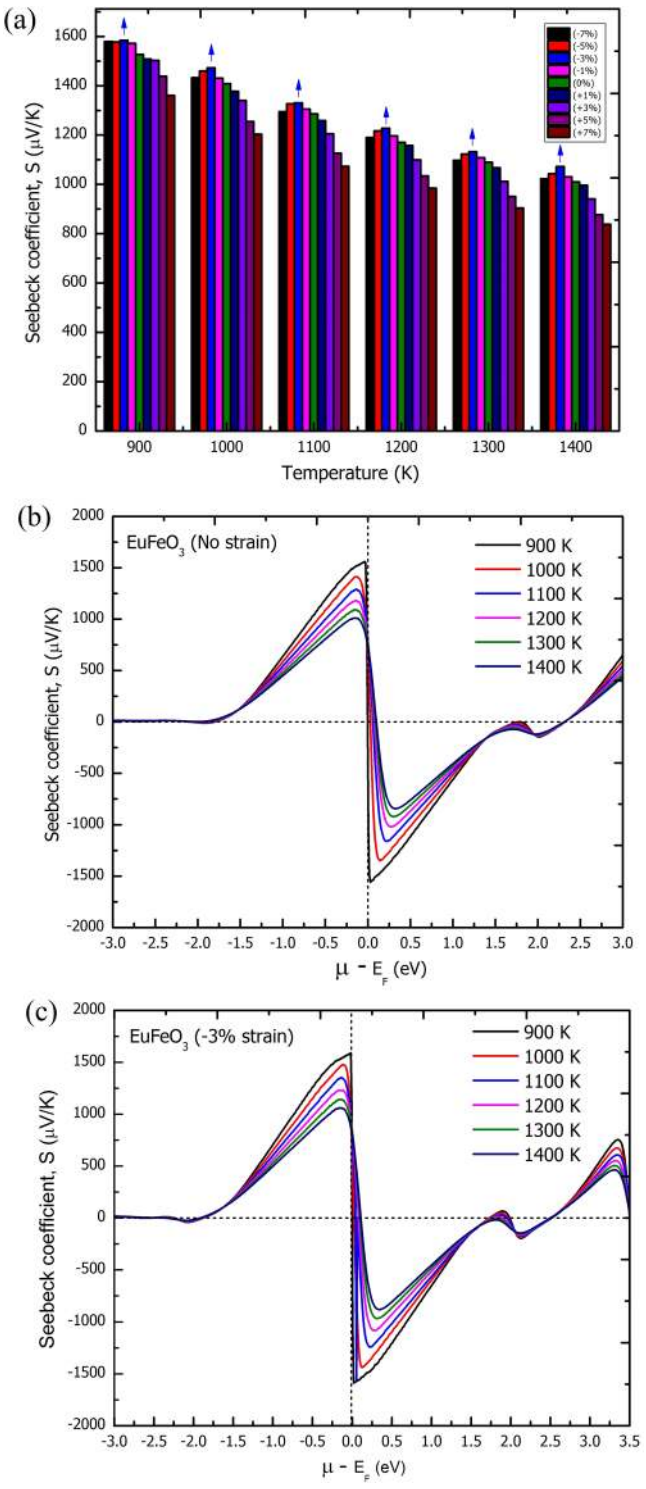

FIG. 3. (a) Seebeck coefficients in $EuFeO_3$ under different values of strains for 900 K ≤ *T* ≤ 1400 K. (b) and (c) Seebeck coefficients with respect to $\mu - E_F$ in $EuFeO_3$ under (b) zero and (c) 3% compressive strains for 900 K ≤ *T* ≤ 1400 K.

changes for 300 K ≤ T ≤ 1400 K under zero strain. Interestingly, we find that S exceeds 1000 μV/K, even for T < 900 K. However, a plateau around $\mu - E_F$ is clearly present where $S = 0$ for the cases where T < 900 K. This distinctive feature implies the presence of a wide bandgap in $EuFeO_3$ that prevents current flow through the material at temperatures lower than 900 K. Apparently, this plateau vanishes at $T \geq 900$, which indicates that electronic excitation becomes easier due to an increase in thermal energy. Therefore, this poses a requirement of thermal activation for the flow of current. Consequently, it is now clear why a larger S is obtained in $EuFeO_3$ for temperatures beyond 900 K and which makes it an excellent high temperature TE material.

Another equally important factor in achieving high ZT and power factors is the electrical conductivity σ. In the case of semiconducting materials, σ varies due to the density and dynamics of electrons and holes. Figures 4(a) and 4(b) show the behavior of the electrical conductivity per relaxation time (σ/τ_0) in $EuFeO_3$ under zero and 3% compressive strains, respectively. It is demonstrated that the temperature has no significant effect on electrical conductivity, although σ slightly decreases with increasing temperature. Under 3% compressive strain in $EuFeO_3$, σ is more pronounced than the unstrained $EuFeO_3$ at the lower $\mu - E_F$ region around 1.5 eV. However, σ increases from −1.0 eV to −6.0 eV in both cases. Doping, on the other hand, has a clear effect on σ. As shown in

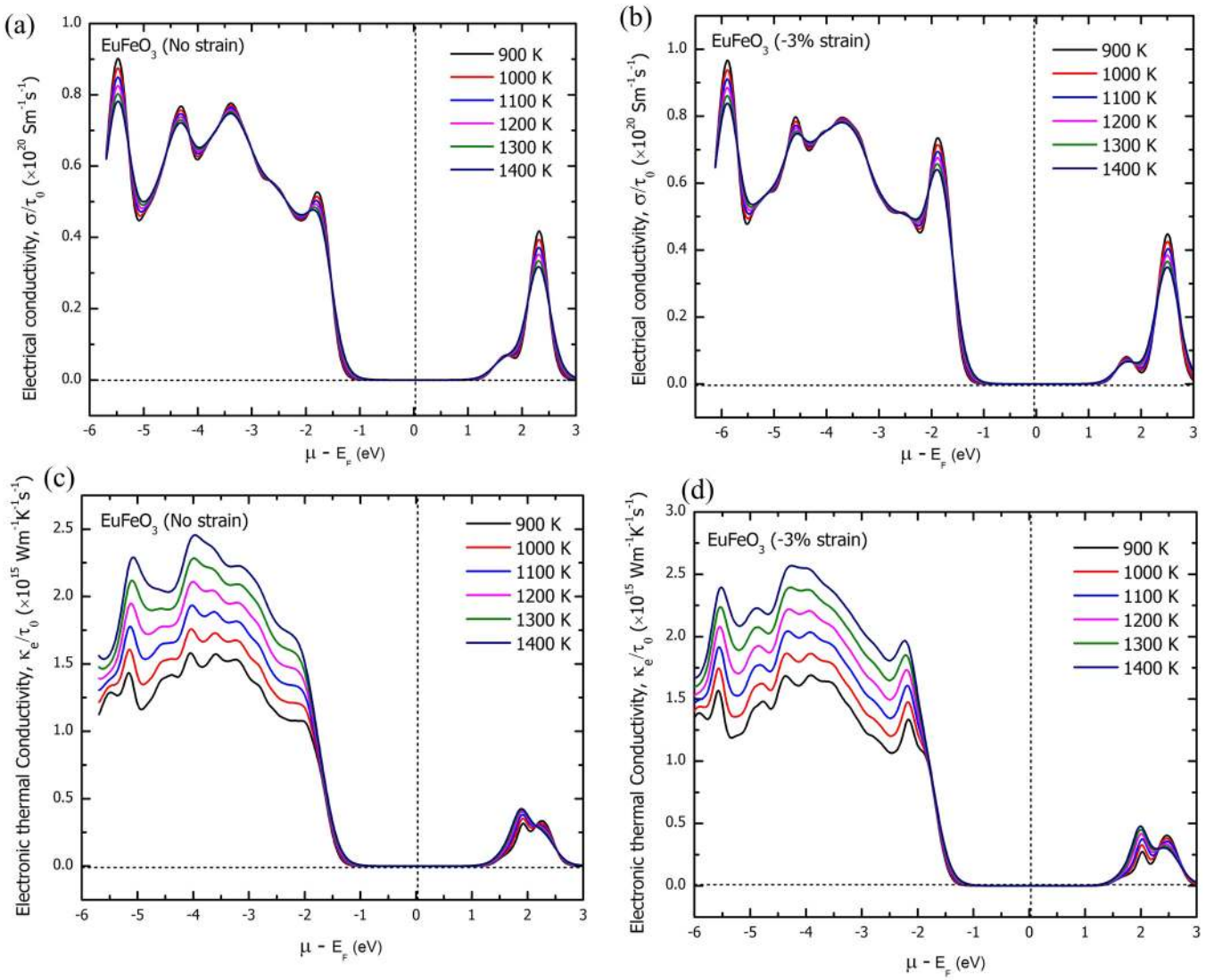

FIG. 4. (a) and (b) Electrical conductivity per relaxation time (σ/τ_0) in $EuFeO_3$ under (a) zero and (b) 3% compressive strains for 900 K ≤ T ≤ 1400 K. (c) and (d) Electronic thermal conductivity per relaxation time (κ_e/τ_0) in $EuFeO_3$ under (c) zero and (d) 3% compressive strains for 900 K ≤ T ≤ 1400 K.

TABLE I. Calculated elastic constants (C_{ij}) required to satisfy the orthorhombic stability conditions of $EuFeO_3$ under zero and compressive strains.

	Strain in $EuFeO_3$			
(C_{ij}) (GPa)	0	−1%	−3%	−5%
C_{11}	286.532 93	296.076 21	309.484 03	325.202 62
C_{12}	128.984 11	143.701 72	174.023 15	204.019 74
C_{13}	119.705 60	129.789 59	150.938 64	176.351 83
C_{22}	268.828 63	282.561 97	305.026 91	327.886 79
C_{23}	125.451 61	132.401 52	147.400 07	167.197 35
C_{33}	272.766 89	285.218 59	311.357 46	341.586 65
C_{44}	109.718 55	112.992 99	118.638 98	125.919 93
C_{55}	88.194 57	92.955 27	101.430 15	110.964 05
C_{66}	76.844 91	84.222 46	100.908 71	119.040 31

Figs. 4(a) and 4(b), p-type doping shows higher electrical conductivities than n-type doping, particularly at energies near the bandgap.

The third factor essential in achieving large *ZT* is the thermal conductivity (κ) of a material. Related to the flow of heat in the materials, κ is broken down into electronic κ_e and lattice thermal conductivities κ_l. The former is primarily due to conduction electrons, while the latter has its origin from lattice phonon vibrations in the material. For a good TE material, it is expected that the thermal conductivity should be sufficiently low as it is inversely proportional to *ZT*. Figures 4(c) and 4(d) show the variation in electronic thermal conductivity (κ_e/τ_0) of $EuFeO_3$ within the temperature range of 900 K to 1400 K under zero and 3% compressive strains, respectively. It is evident that for both cases, κ_e is lower at 900 K. Additionally, we find that as the temperature increases, κ_e also slightly increases. Yet, overall, κ_e does not significantly alter with changes in temperature. We were not able to calculate the lattice contribution to the thermal conductivity, due to the limitation of the Boltztrap2 code that can calculate κ_e only. Nonetheless, we are confident that $EuFeO_3$ should have a relatively high thermopower, due to the presence of extremely flat and corrugated flatbands near the Fermi level and the existence of a wide bandgap. A similar case has also been reported in the TE performance of crystalline cinnabar (α-HgS).[28] If this is so, the increase in the thermopower ultimately contributes to the increase in the high *PF*s. In a higher temperature region, TE materials with high *PF*s would be the right choice rather than looking into the figure of merit (*ZT*). With regard to the lattice thermal conductivity of $EuFeO_3$, previous experimental and lattice-statics simulation studies on the κ_l of $RFeO_3$ materials have shown that it decreases at higher temperatures.[29–31] In our work, we provide the values of κ_l by calculating the theoretical minimum value based on Cahill's method.[32] To estimate this parameter, we first calculated the elastic constants (C_{ij}) and then checked the orthorhombic stability conditions followed by calculating the mechanical and sound/vibrational properties. The MechElastic code[33] was used for this purpose, and the orthorhombic stability conditions[34] were satisfied for $EuFeO_3$ under zero and strained conditions. The calculated elastic constants (C_{ij}) and mechanical properties of $EuFeO_3$ under zero and compressive strains up to 5% are listed in Tables I and II. The omission of calculating these parameters for tensile strains is discussed later in this section. It is clearly perceived that the elastic constants (C_{ij}), mechanical properties, sound/vibrational velocities, and the Debye temperature steadily increased with increasing compressive strain. Once these parameters were obtained, the theoretical minimum lattice thermal conductivity

TABLE II. Calculated mechanical properties, vibrational/sound velocities, Debye temperatures, and theoretical minimum lattice thermal conductivities of $EuFeO_3$ under zero and compressive strains.

		Strain in $EuFeO_3$			
		0	−1%	−3%	−5%
Bulk modulus (GPa)	Voigt	175.157	186.182	207.844	232.202
	Reuss	175.048	186.013	207.628	232.053
	average	175.102	186.098	207.736	232.127
Shear modulus (GPa)	Voigt	85.217	88.565	94.429	100.992
	Reuss	83.338	86.528	90.827	94.117
	average	84.278	87.547	92.628	97.554
Young's modulus (GPa)	Voigt	219.978	229.332	246.029	264.613
	Reuss	215.772	224.738	237.805	248.724
	average	217.875	227.035	241.917	256.668
Poisson ratio	Voigt	0.291	0.295	0.303	0.310
	Reuss	0.295	0.299	0.309	0.321
	average	0.293	0.297	0.306	0.316
Transverse velocity (m/s)		3388.133 00	3418.653 65	3445.447 95	3462.949 81
Longitudinal velocity (m/s)		6257.521 30	6358.171 45	6515.463 85	6672.631 66
Average velocity (m/s)		3780.951 01	3816.952 33	3851.379 37	3875.819 36
Debye temperature (K)		497.670 15	505.789 63	517.341 06	527.907 94
Minimum lattice thermal conductivity (W/m K)		1.4762	1.4946	1.5184	1.5402

($\kappa_{l,min}$) was estimated, as given in Table II. The calculated $\kappa_{l,min}$ was very small (1.4762 W m^{-1} K^{-1} for zero strained $EuFeO_3$) and increased with increasing compressive strain. Given this circumstance, rather than thermal conductivity, we then assert that the power factor (*PF*) is more crucial in generating high thermoelectric power for a given *ZT*.

Recently, it has been discovered that enhancing the *PF* is a clever way of increasing the efficiency and the output power generation.[35] In fact, this approach offers an ingenious technique other than lowering the thermal conductivity. Plots of *PF* per relaxation time ($S^2\sigma/\tau_0$) of $EuFeO_3$ with respect to $\mu - E_F$ under zero and 3% compressive strains are shown in Figs. 5(a) and 5(b), respectively. The *PF* reaches a maximum at the negative chemical potential $\mu - E_F = \sim(-1.4$ eV), and so we considered this point of chemical potential as a critical point for high TE performance of $EuFeO_3$. For positive chemical potentials such as $\mu - E_F = +2.04$ eV and $\mu - E_F = +2.72$ eV, although the calculated *PF*s were considerably high, these values were comparably lower than those obtained for negative chemical potentials. These results confirm that high *PF*s were obtained for p- and n-type doped material, but those obtained for p-type doping were greater. We have therefore chosen to present the thermal and strain dependence of the *PF*s for the case of $\mu - E_F = \sim(-1.4$ eV), where the maximum *PF* was obtained. Figures 5(c) and 5(d) show how the maxima of *PF* ($S^2\sigma/\tau_0$) at

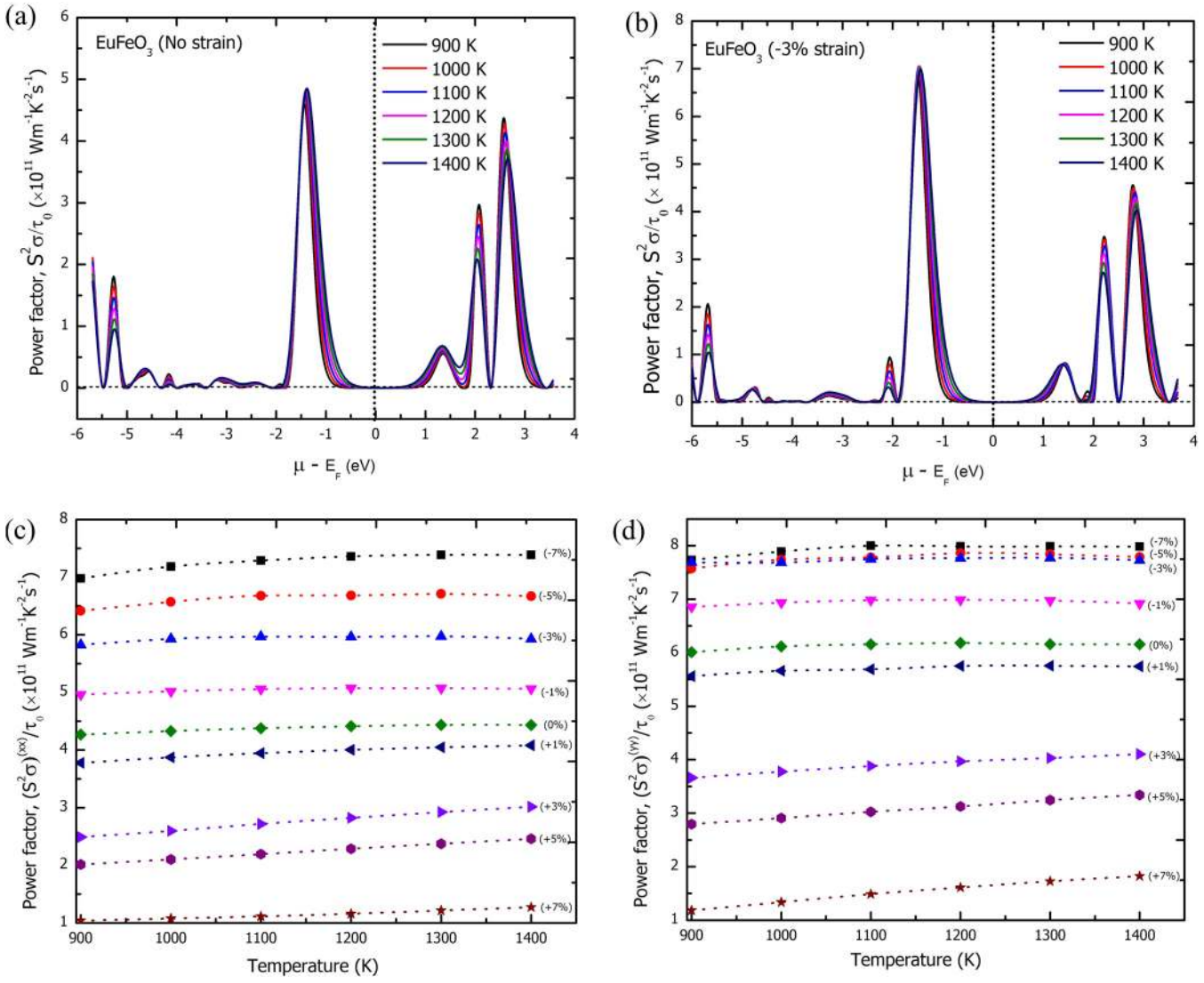

FIG. 5. (a) and (b) Power factor per relaxation time ($S^2\sigma/\tau_0$) in $EuFeO_3$ under (a) zero and (b) 3% compressive strains for 900 K $\leq T \leq$ 1400 K. (c) and (d) Power factor per relaxation time ($S^2\sigma/\tau_0$) at $\mu - E_F = \sim(-1.4$ eV) as a function of temperature for different values of strain in $EuFeO_3$ along the components (c) *xx* and (d) *yy*.

$\mu - E_F = \sim(-1.4$ eV) behaves with respect to temperature for different values of strain along the components (*xx* and *yy*). In these figures, we can immediately infer that the *PF*s are anisotropic in behavior along the *xx* and *yy* components. Here, the *PF* component along *yy* shows higher values than the component along *xx*. On the other hand, the component along *zz* shows similar values of *PF* to the component along *xx*; hence, we did not further investigate the application of strain along the c-axis. Note that the *PF*s are larger along the component *yy* than along the component *xx* in all cases of strain. Remarkably, the effect of the bandgap is also reflected in the *PF* variation brought about by the strain. The bandgap increases as we move from tensile strain (positive) to compressive strain (negative), and the *PF*s also significantly increase. $EuFeO_3$ with a wide bandgap with moderate strain (−3% compressive) turns out to have a better *PF*, which slightly increases with respect to the temperature. The tensile strain shows lower *PF*s than the compressive strain and so we omitted the calculation of elastic constants, mechanical properties, and the theoretical minimum lattice thermal conductivities for the tensile strained $EuFeO_3$ configurations. Also, the lattice thermal conductivity difference between tensile and compressive strain is expected to be only a small difference, which could be realized from the difference between the zero and compressive strained $EuFeO_3$. Although the power factors for 5% and 7% compressive strains appear to be higher than that of the 3% compressive strain due to larger electrical conductivities with increasing compressive strain, the relative total energies of the former strains are comparatively higher than in the ground state. While considering the overall variations with respect to strain, the compressive strain of −3% in $EuFeO_3$ approaching a limiting wide bandgap value shows the highest Seebeck coefficient values, optimal electrical conductivities, and *PF*s in comparison to zero and other strained conditions in $EuFeO_3$.

IV. CONCLUSION

We have found that the presence of corrugated flatbands in the valence band region and the extremely flatbands in the conduction band region in the band structure of $EuFeO_3$ reveal its potential as a thermoelectric material in the high temperature region. This is confirmed from the very high Seebeck coefficients and electrical conductivities, low electronic thermal conductivities, and significantly enhanced power factor values calculated in $EuFeO_3$ under compressive strain. The theoretical minimum lattice conductivity was estimated at around 1.47–1.54 $W\,m^{-1}\,K^{-1}$. $EuFeO_3$ is an experimentally relevant system, and we have predicted that the exceptionally high thermopower and power factors in this wide bandgap semiconducting band structure, with corrugated flat and extremely flatbands arising due to large numbers of unpaired 4f and 3d electrons, could be a breakthrough in the field of high temperature thermoelectric materials.

SUPPLEMENTARY MATERIAL

See the supplementary material for some of the relevant thermoelectric properties, structural parameters, and density of states discussed in this work.

ACKNOWLEDGMENTS

This research work and the authors Dr. P. Iyyappa Rajan and Dr. Carlos Baldo III were supported by appointments to the Young Scientist Training (YST) Program at the Asia Pacific Center for Theoretical Physics (APCTP) through the Science and Technology Promotion Fund and Lottery Fund of the Korean Government. This work also received additional support from the Korean Local Governments of Gyeongsangbuk-do Province and Pohang City.

DATA AVAILABILITY

The data that support the findings of this work are available within the article and the supplementary material.

REFERENCES

[1]D. M. Rowe, *CRC Handbook of Thermoelectrics* (CRC Press, 1995).
[2]S. Twaha, J. Zhu, Y. Yan, and B. Li, "A comprehensive review of thermoelectric technology: Materials, applications, modelling and performance improvement," Renew. Sust. Energy Rev. **65**, 698–726 (2016).
[3]J. W. Fergus, "Oxide materials for high temperature thermoelectric energy conversion," J. Eur. Ceram. Soc. **32**, 525–540 (2012).
[4]Y. Yin, B. Tudu, and A. Tiwari, "Recent advances in oxide thermoelectric materials and modules," Vacuum **146**, 356–374 (2017).
[5]T. M. Tritt, "Thermoelectric phenomena, materials and applications," Annu. Rev. Mater. Res. **41**, 433–448 (2011).
[6]Z. Jing, H. Wang, X. Feng, B. Xiao, Y. Ding, K. Wu, and Y. Cheng, "Superior thermoelectric performance of ordered double transition metal MXenes: $Cr_2TiC_2T_2$ (T = -OH or -F)," J. Phys. Chem. Lett. **10**, 5721–5728 (2019).
[7]R. Maity, A. P. Sakhya, A. Dutta, and T. P. Sinha, "Effect of Sm doping on the structural, morphological and dielectric properties of $EuFeO_3$ ceramics," Solid State Sci. **91**, 28–35 (2019).
[8]X. Niu, H. Li, and G. Liu, "Preparation, characterization and photocatalytic properties REFeO3 (RE = Sm, Eu, Gd)," J. Mol. Catal. A-Chem. **232**, 89–93 (2005).
[9]S. Geller and V. B. Bala, "Crystallographic studies of perovskite-like compounds. II. rare earth alluminates," Acta Crystallogr. **9**, 1019–1025 (1956).
[10]G. F. Herrmann, "Magnetic resonances and susceptibility in orthoferrites," Phys. Rev. B **133**(5A), A1334–A1344 (1964).
[11]M. Siemons and U. Simon, "High throughput screening of the propylene and ethanol sensing properties of rare-earth orthoferrites and orthochromites," Sens. Actuator B **126**(1), 181–186 (2007).
[12]A. K. Choquette, C. R. Smith, R. J. Sichel-Tissot, E. J. Moon, M. D. Scafetta, E. Di Gennaro, F. Miletto Granozio, E. Karapetrova, and S. J. May, "Octahedral rotation patterns in strained $EuFeO_3$ and other Pbnm perovskite films: Implications for hybrid improper ferroelectricity," Phys. Rev. B **94**, 024105 (2016).
[13]A. K. Choquette, R. Colby, E. J. Moon, C. M. Schlepütz, M. D. Scafetta, D. J. Keavney, and S. J. May, "Synthesis, structure and spectroscopy of epitaxial $EuFeO_3$ thin films," Cryst. Growth Des. **15**, 1105–1111 (2015).
[14]M. Marezio, J. P. Remeika, and P. D. Dernier, "The crystal chemistry of the rare earth orthoferrites," Acta Cryst. B **26**, 2008–2022 (1970).
[15]G. Kresse and J. Furthmüller, "Efficient iterative schemes for *ab initio* total-energy calculations using a plane-wave basis set," J. Phys. Rev. B. **54**(16), 11169–11186 (1996).
[16]G. Kresse and D. Joubert, "From ultrasoft pseudopotentials to the projector augmented-wave method," Phys. Rev. B **59**(3), 1758–1775 (1999).
[17]P. Blöchl, "Projector augmented-wave method," Phys. Rev. B **50**(24), 17953–17979 (1994).
[18]J. Perdew, K. Burke, and M. Ernzerhof, "Generalized gradient approximation made simple," Phys. Rev. Lett. **77**(18), 3865–3868 (1996).

[19]S. L. Dudarev, G. A. Botton, Y. Y. Savrasov, C. J. Humphreys, and A. P. Sutton, "Electron-energy-loss spectra and the structural stability of nickel oxide: An LSDA + U study," Phys. Rev. B **57**, 1505–1509 (1998).
[20]M. Pugaczowa-Michalska, J. Kaczkowski, and A. Jezierski, "Electronic and magnetic properties of $BiFeO_3$: Gd^{3+}," Ferroelectrics **461**, 85–91 (2014).
[21]W. H. Press, B. P. Flannery, S. A. Teulolsky, and W. T. Vetterling, *Numerical Recipes: The Art of Scientific Computing* (Cambridge University Press, 1986).
[22]G. H. K. Madsen, J. Carrete, and M. J. Verstraete, "Boltztrap2: A program for interpolating band structures and calculating semi-classical transport coefficients," Comput. Phys. Comm. **231**, 140–145 (2018).
[23]Y. Hinuma, G. Pizzi, Y. Kumagai, F. Oba, and I. Tanaka, "Band structure diagram paths based on crystallography," Comput. Mater. Sci. **128**, 140–184 (2017).
[24]J. M. Crowley, J. Tahir-Kheli, and W. A. Goddard III, "Resolution of the band gap prediction problem for materials design," J. Phys. Chem. Lett. **7**, 1198–1203 (2016).
[25]K. Mori K, H. Usui, H. Sakakibara, and K. Kuroki, "Corrugated flat band as an origin of large thermopower in hole doped $PtSb_2$," AIP Adv. **2**, 042108 (2012).
[26]K. H. Lee, M.-W. Oh, H.-S. Kim, W. H. Shin, K. Lee, J.-H. Lim, J. Kim, and S. Kim, "Enhanced thermoelectric transport properties of n-type InSe due to the emergence of the flat band by Si doping," Inorg. Chem. Front. **6**, 1475–1481 (2019).
[27]Y. Zhao, Z. Dai, C. Lian, and S. Meng, "Exotic thermoelectric behavior in nitrogenated Holey graphene," RSC Adv. **7**, 25803–25810 (2017).
[28]Y. Zhao, Z. Dai, C. Lian, S. Zeng, G. Li, J. Ni, and S. Meng, "Low lattice thermal conductivity and good thermoelectric performance of cinnabar," Phys. Rev. Mater. **1**, 065401 (2017).
[29]S. N. Barilo, A. P. Ges, L. E. Soshnikov, and T. V. Smirnova, "Thermal conductivity of rare-earth orthoferrites at reorientation phase transitions," Phys. Status Solidi B **122**(47), 47–52 (1984).
[30]W. Liu, X. Zeng, S. Liu, Y. Zhu, and A. Wu, "Growth and characterization of $LaFeO_3$ crystals," Key Eng. Mater. **602–603**, 27–31 (2014).
[31]A. Chernatynskiy, A. Auguste, B. Steele, J. E. Phillpot, R. W. Grimes, and S. R. Phillpot, "Elastic and thermal properties of hexagonal perovskites," Comput. Mater. Sci. **122**, 139–145 (2016).
[32]D. G. Cahill, S. K. Watson, and R. O. Pohl, "Lower limit to the thermal conductivity of disordered crystals," Phys. Rev. B **46**(10), 6131–6140 (1992).
[33]S. Singh, I. Valencia-Jaime, O. Pavlic, and A. Romero, "Elastic, mechanical, and thermodynamic properties of Bi-Sb binaries: Effect of spin-orbit coupling," Phys. Rev. B **97**, 054108 (2018).
[34]F. Mouhat and F.-X. Coudert, "Necessary and sufficient elastic stability conditions in various crystal systems," Phys. Rev. B **90**, 224104 (2014).
[35]W. Liu, H. S. Kim, Q. Jie, and Z. Ren, "Importance of high power factor in thermoelectric materials for power generation application: A perspective," Scr. Mater. **111**, 3–9 (2016).